Unidirectional Wave Vector Manipulation in Two-Dimensional Space with an All Passive Acoustic Parity-Time-Symmetric Metamaterials Crystal

Tuo Liu,[1] Xuefeng Zhu,[2,*] Fei Chen,[1] Shanjun Liang,[1] and Jie Zhu[1,†]
[1]Department of Mechanical Engineering, The Hong Kong Polytechnic University, Hung Hom, Kowloon, Hong Kong SAR, China
[2]School of Physics, Huazhong University of Science and Technology, Wuhan, Hubei 430074, China

(Received 18 September 2017; published 19 March 2018)

Exploring the concept of non-Hermitian Hamiltonians respecting parity-time symmetry with classical wave systems is of great interest as it enables the experimental investigation of parity-time-symmetric systems through the quantum-classical analogue. Here, we demonstrate unidirectional wave vector manipulation in two-dimensional space, with an all passive acoustic parity-time-symmetric metamaterials crystal. The metamaterials crystal is constructed through interleaving groove- and holey-structured acoustic metamaterials to provide an intrinsic parity-time-symmetric potential that is two-dimensionally extended and curved, which allows the flexible manipulation of unpaired wave vectors. At the transition point from the unbroken to broken parity-time symmetry phase, the unidirectional sound focusing effect (along with reflectionless acoustic transparency in the opposite direction) is experimentally realized over the spectrum. This demonstration confirms the capability of passive acoustic systems to carry the experimental studies on general parity-time symmetry physics and further reveals the unique functionalities enabled by the judiciously tailored unidirectional wave vectors in space.

DOI: 10.1103/PhysRevLett.120.124502

In 1998, Bender and Boettcher [1] extended the conventional quantum mechanics into a complex domain and proposed the concept of space-time reflection symmetry, or parity-time (PT) symmetry, for the non-Hermitian Hamiltonians with real spectra. PT-related theories have since been intensively investigated with optical systems, based on the equivalence between the Schrödinger equation and the classical wave equation [2,3]. It has been proved that a PT-symmetric Hamiltonian is in its unbroken PT-symmetry phase if its eigenfunctions are also those of the PT operator [4–6]. To respect PT symmetry, a necessary (but not sufficient) condition is that the Hamiltonian potential is even in its real part and odd in its imaginary part in space. As the amplitude of the imaginary part goes beyond a threshold, a transition from the unbroken to broken PT symmetry phase can be observed, in which the real energy spectrum becomes complex abruptly. Such threshold corresponds to an exceptional point or a spontaneous breakdown point of PT symmetry, where the amplitudes of the real and imaginary parts are identical. In the past several years, much effort has been dedicated to the realization of PT-synthetic medium [5,6], which possesses the required complex PT-symmetric potentials through balanced gain-loss modulation. Unconventional phenomena, such as Bloch oscillations [7,8], unidirectional invisibility or reflectionlessness [9–13], coherent perfect absorption [14–16], single-mode or vortex lasing [17–19], and low-power light-light switching [20], have been subsequently demonstrated. However, the experimental investigations of PT-synthetic optical media are hitherto based on one-dimensional (1D) waveguides, in which the wave propagation direction is parallel or perpendicular to the PT potential. PT symmetry in higher-dimensional space has only been theoretically discussed [21–26].

Acoustic PT-symmetric systems [27–32], albeit in an early stage, have exhibited significant value in many aspects, including one-way cloak [27], invisible sensing [28], and phonon lasing [31]. Still, those designs followed the similar approach of 1D gain-loss dimer configuration. To overcome the absence of acoustic gain medium in nature, active sound generating unit [28,29,33], or additional fluid field [32] has been applied to provide wave amplification in experiment, but the complex circuit and external energy supply requirement inevitably reduce the robustness and usability. Nevertheless, airborne sound shows great flexibility in expanding PT symmetry in higher-dimensional space due to its longitudinal wave nature, as well as the zero cutoff within waveguides.

To demonstrate the capability of a passive acoustic system to carry the PT symmetry study and tailor the associated unpaired wave vectors in 2D space, we show here the realization of unidirectional sound focusing, with an all passive acoustic PT-symmetric metamaterials crystal [34]. Metamaterials, artificially structured on subwavelength scale to obtain exotic properties absent in nature, have enabled many extraordinary ways of wave manipulation [35–37]. For our design, as depicted in Fig. 1, the acoustic PT-symmetric material is constructed through periodically interleaving two different passive metastructures, the groove- and holey-structured metamaterials,

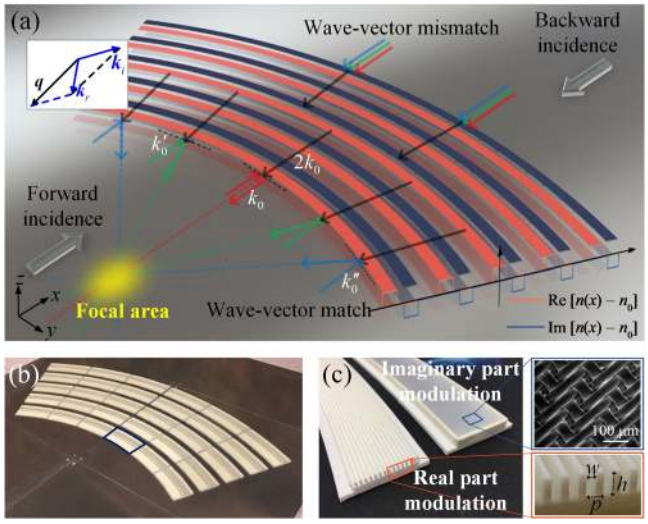

FIG. 1. All passive acoustic PT-symmetric metamaterials crystal. (a) Unidirectional focusing based on directional wave-vector matching. The upper-left inset is an illustration of the specular reflection induced by wave-vector matching $\boldsymbol{k}_r = \boldsymbol{q} + \boldsymbol{k}_i$ ($|\boldsymbol{k}_i| = |\boldsymbol{k}_r|$) in 2D space. For different frequencies k_0(red) $<$ k_0'(green) $<$ k_0''(blue), such reflections exist at different areas along the arc, so that the reflected waves are focused within a small zone. $\boldsymbol{q}$ does not provide any wave-vector matching for backward incidence, thus leading to no reflection. (b) The fabricated passive acoustic PT-symmetric metamaterials crystal. The circumferential opening angle 60° in the x–y plane is divided into six segments of equal opening angle 9.7°. (c) The real and imaginary part modulations. Each individual modulation is $T/2 = 30$ mm in length within a planar waveguide of height $H =$ 20 mm [39]. The real part modulation: 3D-printed groove-structured metamaterials of opening width $w = 1.2$ mm, depth $h = 3$ mm, and interval $p = 2$ mm (lower-right inset: enlarged photo). The imaginary part modulation: holey-structured metamaterials, viz., the 60-μm-thick mesh fabrics (upper-right inset: scanning electron microscope image). The average pore size and open area are 7 μm and 2%. Its acoustic impedance is about 4000 Pa s/m.

along the radial direction inside an acoustic waveguide. Arranged in the form of a 2D circumferentially expanded Bragg reflector within the annular sector region, it provides balanced real and imaginary part modulations, required by the passive PT-symmetric system, to the refractive index. This complex modulation offers a unidirectional wave vector [9,12] $\boldsymbol{q} = -2k_B\boldsymbol{r}/r$ toward the sector center, where k_B is the wave number at the Bragg frequency f_B. For the 1D scenario [9,12], when the frequency f is deviated away from f_B, the incidence wave vector $\boldsymbol{k}_i$, the reflection wave vector $\boldsymbol{k}_r$, and the unidirectional wave vector $\boldsymbol{q}$ provided by the complex modulation are mismatched for forward and backward incidences, leading to a trivial effect of bidirectional reflectionlessness. When the system operates at f_B, the wave-vector matching condition $\boldsymbol{k}_r = \boldsymbol{q} + \boldsymbol{k}_i$ ($|\boldsymbol{k}_i| = |\boldsymbol{k}_r| = k_B$) is satisfied only along the forward direction, giving rise to a nontrivial effect of unidirectional reflectionlessness. For our passive acoustic PT-symmetric metamaterials crystal, the wave-vector matching obeys the rule of 2D vector addition [38]; thus, strong specular reflection occurs at particular positions where $\boldsymbol{k}_i$, $\boldsymbol{k}_r$, and $\boldsymbol{q}$ (not necessarily parallel) become matched [the inset of Fig. 1(a)], allowing a possibly higher reflection frequency ($|\boldsymbol{k}_i| + |\boldsymbol{k}_r| > |\boldsymbol{q}|$, when $f > f_B$), so that the unidirectional focusing can be observed over the spectrum. Note that such wave-vector match does not require the incident angle to be small with respect to $\boldsymbol{q}$ [39]. Hence, it is not the simple case of paraxial wave propagation in 1D PT-symmetric medium, but rather a physical problem of interactions between incident waves and PT-symmetric potential in 2D space. The resultant PT potential goes beyond the gain-loss dimer configuration, generating equivalent unpaired wave vectors to enable unidirectional reflectionlessness (along with acoustic transparency) and one-way focusing over a considerable bandwidth.

The evolution from the exact to the passive PT-symmetric modulation along the radial direction is presented in Fig. 2(a). The PT-symmetric modulation of the refractive index is given in a generalized form $\Delta n(x) = n(x) - n_0 = n' \cos(qx) + i\delta n' \sin(qx)$ with $n' \ll n_0$, where n_0, n', and δ denote the background refractive index, modulation amplitude, and modulation ratio, respectively. The complex

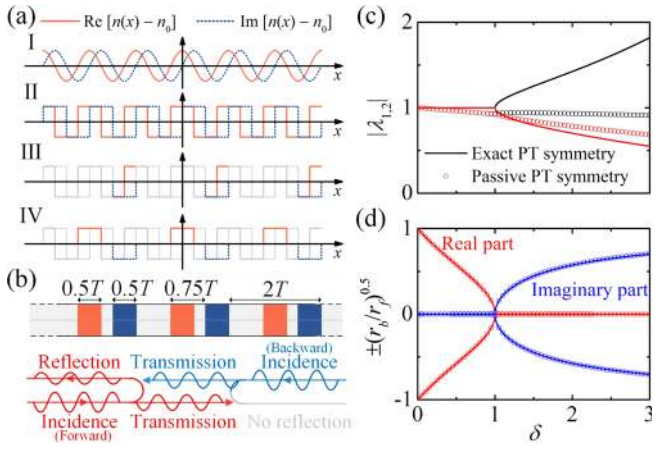

FIG. 2. Exact and passive acoustic PT-symmetric potentials. (a) Evolution of the acoustic PT-symmetric potential through refractive index modulations: I. Exact PT-symmetric potential (complex exponential modulation) → II. Exact PT-symmetric potential (complex square-wave modulation) → III. Passive PT-symmetric potential (truncated complex square-wave modulation) → IV. Passive PT-symmetric potential ($3\pi/2$ in phase shift of the real part modulation). The red (blue) curves denote the real (imaginary) part modulations. (b) Arrangement of the real part and imaginary part refractive index modulators. The modulation period is $T_m = 2T$. (c) Absolute value of the eigenvalues and (d) the second term of the eigenvectors of the scattering matrix, where lines and circles correspond to exact and passive PT-symmetric potentials [II and IV in (a)]. During the calculations, the modulation amplitude is set as $n' = 0.001n_0$ and the total length $L = 100T$, with operating frequency being the Bragg frequency.

exponential modulation can be replaced with a complex square-wave modulation [I → II, Fig. 2(a)] to simplify the structural design requirement [27]. Alternatively, the complex exponential modulation can be regarded as the first-order Fourier expansion of a complex square-wave modulation. Because of the absence of natural gain medium for sound, the complex square-wave modulation is truncated by only considering $x \in [4m\pi/q + \pi/q, 4m\pi/q + 2\pi/q]$. After truncation [II → III, Fig. 2(a)], only one negative half cycle out of two periods of the imaginary part modulation is retained, making the modulation period doubled (from $T = 2\pi/q$ to $2T = 4\pi/q$), where we focus on the second-order Bragg scattering [12]. This treatment leaves us sufficient space to further conduct an in-phase shift of the real part modulation, so that the overlap between the real and imaginary parts can be spatially separated, as we will present later. If we apply the Fourier transformation to the exact and passive square-wave modulations as $\Delta n(x)/n' = C_q \exp(iqx) + C_{-q} \exp(-iqx) + C_0$, we may find that there exists a factor of 4 in the coefficients C_q and C_{-q} between these two modulations [39]. In a weak coupling regime, the scattering matrix subject to such passive PT-symmetric potential can be derived based on the coupled-mode theory. The associated eigenvalues $\lambda_{1,2} = t \pm \sqrt{r_f r_b}$, where t, r_f, and r_b denote the transmission and forward- and backward-reflection coefficients, can be expressed as [39]

$$\lambda_{1,2} = a\lambda'_{1,2} = a\frac{1 \pm i\frac{1}{2\pi}\frac{\kappa}{\gamma}\sinh(\gamma L)\sqrt{1-\delta^2}}{\sqrt{1+\frac{1}{4\pi^2}\frac{\kappa^2}{\gamma^2}\sinh^2(\gamma L)(1-\delta^2)}}, \tag{1}$$

with

$$a = \frac{\sqrt{1+\frac{1}{4\pi^2}\frac{\kappa^2}{\gamma^2}\sinh^2(\gamma L)(1-\delta^2)}}{\cosh(\gamma L) - \frac{\delta}{4}\frac{\alpha}{\gamma}\sinh(\gamma L)},$$

$$\gamma = \sqrt{(\delta\alpha/4)^2 + (1-\delta^2)\kappa^2/4\pi^2}.$$

Here, α is the attenuation coefficient inside the modulated region and κ is the coupling coefficient between forward and backward propagating modes. Evidently, the eigenspectrum of the passive PT-symmetric system ($\lambda_{1,2}$) is the exact PT-symmetric system ($\lambda'_{1,2}$) multiplied by a factor $a < 1$ that offsets the eigenvalues toward losses. When $0 \le \delta < 1$, $\lambda'_{1,2}$ are conjugated and unimodular. The system operates in the passive unbroken PT symmetry phase. When $\delta > 1$, $\lambda'_{1,2}$ are nonunimodular with a pair of reciprocal moduli. The system operates in the passive broken PT symmetry phase. When $\delta = 1$, the eigenvalues become degenerate with $\lambda_{1,2} = a = \exp(-\alpha L/4)$. In this case, similar to the phase transition point from the unbroken to broken PT symmetry phase in an exact PT-symmetric system, the passive PT-symmetric system experiences an exceptional point where a π phase shift occurs with backward reflection vanished. The real part modulation is then shifted $3\pi/2$ in phase to eliminate its overlap with the imaginary part modulation [III → IV, Fig. 2(a)]. It allows a more practical construction of the passive PT-symmetric system as we may now design the real and imaginary part modulators independently. The absolute value of $\lambda_{1,2} = t \pm \sqrt{r_f r_b}$ and the second components of the eigenvectors $(1 \quad \pm\sqrt{r_b/r_f})^T$ for both the exact and passive PT-symmetric systems [II and IV, Fig. 2(a)] are calculated using the transfer matrix method [39]. In Fig. 2(c), $|\lambda_1|$ and $|\lambda_2|$ overlap (conjugate eigenvalues) in exact or passive unbroken PT symmetry phase ($0 \le \delta < 1$), degenerate at the exceptional point ($\delta = 1$), and are unequal in exact or passive broken PT symmetry phase ($\delta > 1$). This is further confirmed by Fig. 2(d), where $\pm\sqrt{r_b/r_f}$ are either purely real at $0 \le \delta < 1$ or purely imaginary at $\delta > 1$ [27]. The results show similar characteristics in PT phase evolution between the two systems.

By curling such 1D passive PT-symmetric potential circumferentially, the resulted medium can offer radial unidirectional wave vectors in the global coordinates for incoming waves [39], equivalent to the exact PT-symmetric modulation of the refractive index $\Delta n(r) = n' \exp[iq(r - r_0)]$, where r_0 is the starting radius of the PT-symmetric potential sector. The passive PT-symmetric metamaterials crystal is constructed using two paralleled rigid plates carved with curved slot openings to install the refractive index modulators [39]. The real part modulation is realized by the 3D-printed groove-structured metamaterials shown in Fig. 1(c), well known for its capability to decelerate sound waves. The effective loss for the imaginary part modulation can be accomplished through purposely introduced sound leakage, similar to the radiation losses in optics [45]. Slit structures have been proposed for such purpose, but with the downside of strong dispersion [29]. Instead, we go with the holey-structured acoustic metamaterials, viz., commercial mesh fabrics shown in Fig. 1(c). Their homogeneously distributed deep-subwavelength pores guarantee sufficiently high acoustic resistance-reactance ratio and precise leakage control, leading to almost nondispersive loss. It would enable the approximately balanced modulation required by the exceptional point in a broader bandwidth.

We conducted full-wave simulations and experiments to test the hypothesis. The modulation amplitude and period are set as $n' = 0.05n_0$ and $2T = 120$ mm. During the measurement [39], a loudspeaker array is employed to generate plane waves. The sound fields are scanned by a 3-mm-diameter microphone. Figure 3(a) presents the normalized sound energy density fields for forward and backward incidences at 3000 Hz, in which the simulated and measured results agree well. Remarkable contrast in opposite directions can be observed from the different interference patterns within the measurement areas, marked by the white boxes. To validate that the focusing effect is indeed from the unidirectional wave vectors offered by our

passive PT-symmetric metamaterials crystal, rather than from the geometric shape of the entire concave surface, the measured sound pressure distributions at different frequencies along $y = 0$ are presented in Fig. 3(b). The overall amplitude of the standing-wave fields is frequency dependent for forward incidence [Fig. 3(b), the upper panel], while being almost frequency independent for backward incidence [Fig. 3(b), the lower panel]. It can be inferred that, when the passive PT-symmetric metamaterials crystal is replaced by a rigid concave reflector, the overall amplitude of both the forward and backward standing-wave fields would be frequency independent within the studied spectrum [39]. At the exceptional point, the system is strongly reflective from one side, but nearly reflectionless from the other. Here, the forward and backward standing-wave ratios G_f and G_b, viz., the ratio between the peak and valley values of the standing-wave fields [Fig. 3(c)], are extracted as indicators to evaluate the reflection strengths. The contrast ratio G_f/G_b plotted in Fig. 3(d) can thus be used to estimate the difference between the forward and backward reflections. Note that the interference pattern is a result of the superposition between the incident and reflected waves propagating in all possible directions. To reduce the disturbance of reflections from the positions at $y \neq 0$, we chose to extract G_f away from the focal spot, where the reflected waves diverge and the normal reflection along $y = 0$ dominates. In Fig. 3(d), the peak shows that the contrast between forward and backward reflections along the x direction reaches maximum, which occurs nearby the exceptional point. A slight red shift of the Bragg frequency (from 2858 to 2820 Hz) is caused by the increased overall refractive index after $3\pi/2$ in phase shift of the real part modulation. Another way to further confirm this one-way wave-vector matching behavior is by simply reversing the directions of the complex refractive index modulation, that is, by switching the reflective and the reflectionless sides. In this scenario, the concave surface would merely generate a very weak focusing effect [39].

The acoustic focusing effect over the spectrum enabled by directional wave-vector matching is further examined in the simulated scattered sound energy density fields of Fig. 4(a). At 2500 Hz, lower than f_B, the large wave-vector mismatch hardly induces any reflection for the forward incidence. When f approaches and eventually surpasses f_B, the wave-vector matching condition is approximately satisfied within the 2D plane, giving rise to clear reflections and focused

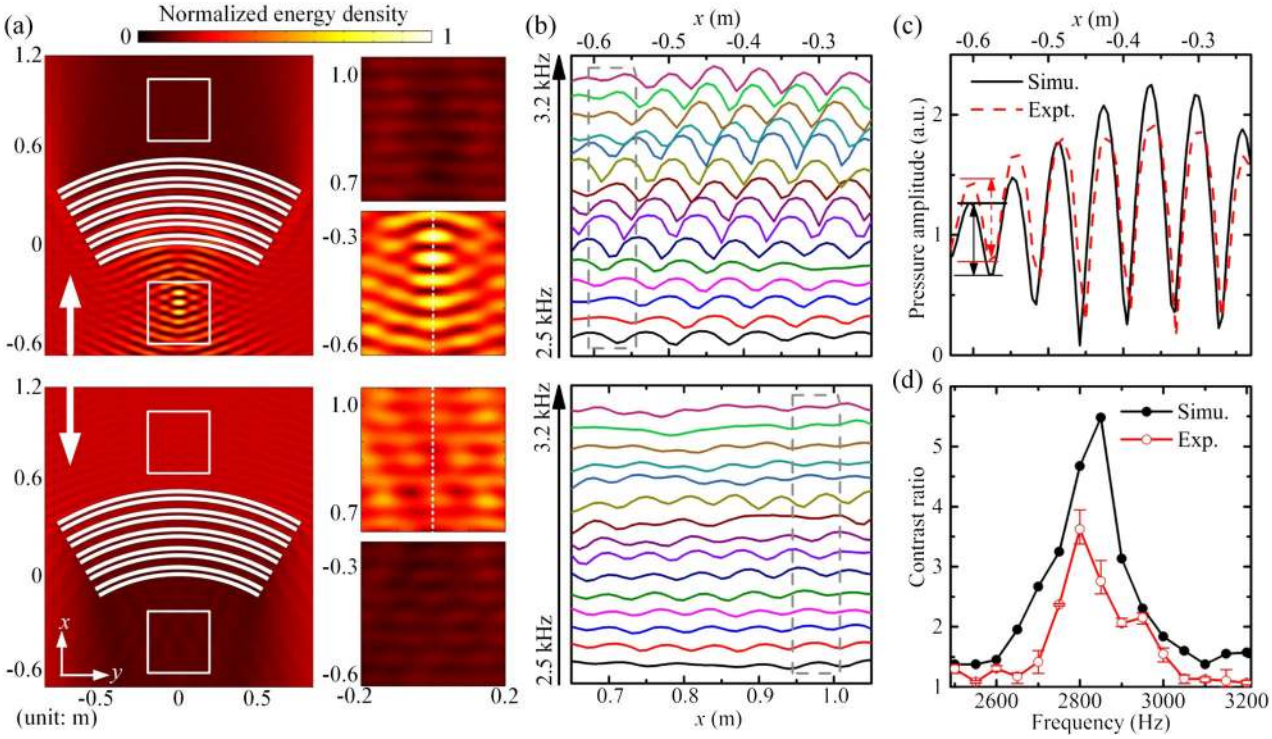

FIG. 3. Unidirectional sound reflection and focusing. (a) Simulated (left) and measured (right) acoustic energy density fields for the forward (upper) and backward (lower) incidences at 3000 Hz. The white boxes mark the measurement areas. The arrows denote incidence directions. (b) Absolute acoustic pressure distributions for forward (upper) and backward (lower) incidences, along the white dashed lines marked in (a), from 2500 to 3200 Hz, with 50 Hz stepping. The dashed rectangles indicate the areas where the standing-wave ratios G_f and G_b are extracted ($x = -0.55$ to -0.63 m and $x = 0.94$–1.02 m). (c) Simulated and measured standing-wave patterns at 3000 Hz for the forward incidence. The red (black) arrow marks the peak and valley that we employ to calculate $G_f = p_{\text{peak}}/p_{\text{valley}}$ in experiment (simulation). The extraction of G_b follows the same process. (d) Extracted contrast ratio G_f/G_b versus frequency. The error bars are generated from four repeated measurements.

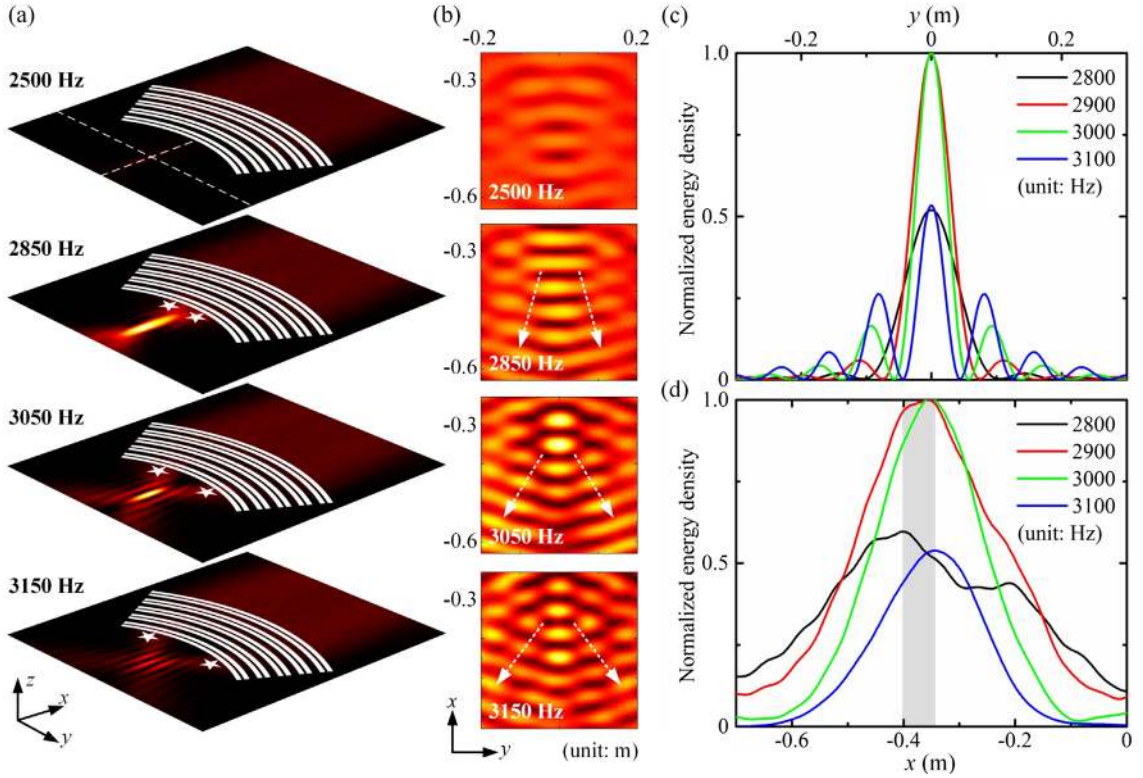

FIG. 4. Unidirectional sound focusing over spectrum. (a) Simulated scattered energy density fields at 2500, 2850, 3050, and 3150 Hz. For forward incidences at different frequencies, strong reflections occur at different locations, marked by the white asterisks, to form focal areas. (b) Measured total energy density fields for the forward incidence at frequencies shown in (a). The interference pattern varies with frequency due to the change of reflected wave front normal, indicated by the white arrows. (c),(d) Simulated scattered energy density distributions along the dashed lines $x = -350$ mm and $y = 0$ mm in (a). All the curves are normalized per the maximum. The shadow area in (d) indicates the spatial range of focal zones at multiple frequencies.

sound field. The measured interference patterns in Fig. 4(b) prove this frequency-dependent reflection wave front change, consistent with the simulation results. The simulated energy density distributions along the dashed lines in Fig. 4(a) are displayed in Figs. 4(c) and 4(d) for multiple operating frequencies. Clearly, the focal spots are located within a small area over the spectrum.

In conclusion, complex modulation of the refractive index enables the study of *PT* symmetry with acoustic systems. In contrast to the balanced gain-loss configurations that require gain medium or external intervention, our all passive acoustic metamaterials crystal provides intrinsic *PT*-symmetric potential to generate unpaired wave vectors via refractive index modulation in a complex domain. By expanding the potential in 2D space, we demonstrate the exceptional point and the unidirectional sound focusing effect (along with reflectionless acoustic transparency in the opposite direction) over a certain spectrum. Moreover, the absence of cutoff in such acoustic *PT*-symmetric system makes the extension of general *PT* symmetry study in multidimensional space highly feasible. To further construct a genuine 2D passive *PT*-symmetric material, we may combine multiple passive *PT*-symmetric potentials into one region, so that the material can simultaneously offer differently oriented unpaired wave vectors [39]. Our study not only provides a new degree of freedom to the realization of unique wave dynamics for applications like noise control, acoustic sensing, and imaging, but also paves the way toward practical investigation of other quantum-analogue phenomena.

The work was supported by the Early Career Scheme (ECS) of Hong Kong RGC (Grant No. 25208115). X. Z. acknowledges support from National Natural Science Foundation of China (Grants No. 11690030, No. 11690032, and No. 11674119). We thank Mannian Yang and Saati Technical Fabric (Tianjin) Co. Ltd. for providing the mesh fabrics samples.

T. L. and X. Z. contributed equally to this work.

*Corresponding author.
xfzhu@hust.edu.cn
†Corresponding author.
jiezhu@polyu.edu.hk

[1] C. M. Bender and S. Boettcher, Real Spectra in Non-Hermitian Hamiltonians Having *PT* Symmetry, Phys. Rev. Lett. **80**, 5243 (1998).

[2] C. M. Bender, D. C. Brody, and H. F. Jones, Complex Extension of Quantum Mechanics, Phys. Rev. Lett. **89**, 270401 (2002).
[3] C. M. Bender, Making sense of non-Hermitian Hamiltonians, Rep. Prog. Phys. **70**, 947 (2007).
[4] K. G. Makris, R. El-Ganainy, D. N. Christodoulides, and Z. H. Musslimani, Beam Dynamics in *PT* Symmetric Optical Lattices, Phys. Rev. Lett. **100**, 103904 (2008).
[5] A. Guo, G. J. Salamo, D. Duchesne, R. Morandotti, M. Volatier-Ravat, V. Aimez, G. A. Siviloglou, and D. N. Christodoulides, Observation of *PT*-Symmetry Breaking in Complex Optical Potentials, Phys. Rev. Lett. **103**, 093902 (2009).
[6] C. E. Rüter, K. G. Makris, R. El-Ganainy, D. N. Christodoulides, M. Segev, and D. Kip, Observation of parity-time symmetry in optics, Nat. Phys. **6**, 192 (2010).
[7] S. Longhi, Bloch Oscillations in Complex Crystals with *PT* Symmetry, Phys. Rev. Lett. **103**, 123601 (2009).
[8] Y. L. Xu, W. S. Fegadolli, L. Gan, M. H. Lu, X. P. Liu, Z. Y. Li, A. Scherer, and Y. F. Chen, Experimental realization of Bloch oscillations in a parity-time synthetic silicon photonic lattice, Nat. Commun. **7**, 11319 (2016).
[9] Z. Lin, H. Ramezani, T. Eichelkraut, T. Kottos, H. Cao, and D. N. Christodoulides, Unidirectional Invisibility Induced by *PT*-Symmetric Periodic Structures, Phys. Rev. Lett. **106**, 213901 (2011).
[10] A. Regensburger, C. Bersch, M. A. Miri, G. Onishchukov, D. N. Christodoulides, and U. Peschel, Parity-time synthetic photonic lattices, Nature (London) **488**, 167 (2012).
[11] L. Ge, Y. D. Chong, and A. D. Stone, Conservation relations and anisotropic transmission resonances in one-dimensional *PT*-symmetric photonic heterostructures, Phys. Rev. A **85**, 023802 (2012).
[12] L. Feng, Y. L. Xu, W. S. Fegadolli, M. H. Lu, J. E. Oliveira, V. R. Almeida, Y. F. Chen, and A. Scherer, Experimental demonstration of a unidirectional reflectionless parity-time metamaterial at optical frequencies, Nat. Mater. **12**, 108 (2013).
[13] B. Peng, Ş. K. Özdemir, F. Lei, F. Monifi, M. Gianfreda, G. L. Long, S. Fan, F. Nori, C. M. Bender, and L. Yang, Parity-time-symmetric whispering-gallery microcavities, Nat. Phys. **10**, 394 (2014).
[14] S. Longhi, *PT*-symmetric laser absorber, Phys. Rev. A **82**, 031801 (2010).
[15] Y. D. Chong, L. Ge, and A. D. Stone, *PT*-Symmetry Breaking and Laser-Absorber Modes in Optical Scattering Systems, Phys. Rev. Lett. **106**, 093902 (2011).
[16] Y. Sun, W. Tan, H. Q. Li, J. Li, and H. Chen, Experimental Demonstration of a Coherent Perfect Absorber with *PT* Phase Transition, Phys. Rev. Lett. **112**, 143903 (2014).
[17] L. Feng, Z. J. Wong, R. M. Ma, Y. Wang, and X. Zhang, Single-mode laser by parity-time symmetry breaking, Science **346**, 972 (2014).
[18] H. Hodaei, M. A. Miri, M. Heinrich, D. N. Christodoulides, and M. Khajavikhan, Parity-time-symmetric microring lasers, Science **346**, 975 (2014).
[19] P. Miao, Z. Zhang, J. Sun, W. Walasik, S. Longhi, N. M. Litchinitser, and L. Feng, Orbital angular momentum microlaser, Science **353**, 464 (2016).
[20] H. Zhao, W. S. Fegadolli, J. Yu, Z. Zhang, L. Ge, A. Scherer, and L. Feng, Metawaveguide for Asymmetric Interferometric Light-Light Switching, Phys. Rev. Lett. **117**, 193901 (2016).
[21] C. M. Bender and D. J. Weir, Phase transition in multidimensional quantum systems, J. Phys. A **45**, 425303 (2012).
[22] C. M. Bender, M. Gianfreda, and S. P. Klevansky, Systems of coupled *PT*-symmetric oscillators, Phys. Rev. A **90**, 022114 (2014).
[23] L. Ge and A. D. Stone, Parity-Time Symmetry Breaking Beyond One Dimension: The Role of Degeneracy, Phys. Rev. X **4**, 031011 (2014).
[24] M. Turduev, M. Botey, I. Giden, R. Herrero, H. Kurt, E. Ozbay, and K. Staliunas, Two-dimensional complex parity-time-symmetric photonic structures, Phys. Rev. A **91**, 023825 (2015).
[25] H. Benisty, A. Lupu, and A. Degiron, Transverse periodic *PT* symmetry for modal demultiplexing in optical waveguides, Phys. Rev. A **91**, 053825 (2015).
[26] W. W. Ahmed, R. Herrero, M. Botey, and K. Staliunas, Locally parity-time-symmetric and globally parity-symmetric systems, Phys. Rev. A **94**, 053819 (2016).
[27] X. Zhu, H. Ramezani, C. Shi, J. Zhu, and X. Zhang, *PT*-Symmetric Acoustics, Phys. Rev. X **4**, 031042 (2014).
[28] R. Fleury, D. Sounas, and A. Alù, An invisible acoustic sensor based on parity-time symmetry, Nat. Commun. **6**, 5905 (2015).
[29] C. Shi, M. Dubois, Y. Chen, L. Cheng, H. Ramezani, Y. Wang, and X. Zhang, Accessing the exceptional points of parity-time symmetric acoustics, Nat. Commun. **7**, 11110 (2016).
[30] J. Christensen, M. Willatzen, V. R. Velasco, and M. H. Lu, Parity-Time Synthetic Phononic Media, Phys. Rev. Lett. **116**, 207601 (2016).
[31] A. V. Poshakinskiy, A. N. Poddubny, and A. Fainstein, Multiple Quantum Wells for *PT*-Symmetric Phononic Crystals, Phys. Rev. Lett. **117**, 224302 (2016).
[32] Y. Aurégan and V. Pagneux, *PT*-Symmetric Scattering in Flow Duct Acoustics, Phys. Rev. Lett. **118**, 174301 (2017).
[33] B. I. Popa and S. A. Cummer, Non-reciprocal and highly nonlinear active acoustic metamaterials, Nat. Commun. **5**, 3398 (2014).
[34] A. Salandrino and N. Engheta, Far-field subdiffraction optical microscopy using metamaterial crystals: Theory and simulations, Phys. Rev. B **74**, 075103 (2006).
[35] Z. Liu, X. Zhang, Y. Mao, Y. Y. Zhu, Z. Yang, C. T. Chan, and P. Sheng, Locally resonant sonic materials, Science **289**, 1734 (2000).
[36] N. Fang, H. Lee, C. Sun, and X. Zhang, Sub-diffraction-limited optical imaging with a silver superlens, Science **308**, 534 (2005).
[37] N. Kaina, F. Lemoult, M. Fink, and G. Lerosey, Negative refractive index and acoustic superlens from multiple scattering in single negative metamaterials, Nature (London) **525**, 77 (2015).
[38] X. Zhu, L. Feng, P. Zhang, X. Yin, and X. Zhang, One-way invisible cloak using parity-time symmetric transformation optics, Opt. Lett. **38**, 2821 (2013).

[39] See Supplemental Material at http://link.aps.org/supplemental/10.1103/PhysRevLett.120.124502 for theory, metamaterials design, additional simulations, sample fabrication, and experimental setup, which includes Ref. [40–44].
[40] J. W. S. B. Rayleigh, *The Theory of Sound* (MacMillan, London, 1929), 2nd ed., Vol. 2, p. 333.
[41] G. Kirchhoff, Ueber den Einfluss der Wärmeleitung in einem Gase auf die Schallbewegung, Ann. Phys. **210**, 177 (1868).
[42] C. Zwikker and C. W. Kosten, *Sound Absorbing Materials* (Elsevier, Amsterdam, 1949), Chap. 2.
[43] D. Y. Maa, Potential of microperforated panel absorber, J. Acoust. Soc. Am. **104**, 2861 (1998).
[44] V. Fokin, M. Ambati, C. Sun, and X. Zhang, Method for retrieving effective properties of locally resonant acoustic metamaterials, Phys. Rev. B **76**, 144302 (2007).
[45] R. Ferrini, R. Houdré, H. Benisty, M. Qiu, and J. Moosburger, Radiation losses in planar photonic crystals: Two-dimensional representation of hole depth and shape by an imaginary dielectric constant, J. Opt. Soc. Am. B **20**, 469 (2003).